

# The effects of fibre spatial distribution and relative orientation on the percolation and mechanics of stochastic fibre networks: A model of peptide hydrogels

Amir Hossein Namdar<sup>1</sup>, Nastaran Zoghi<sup>2</sup>, Aline Miller<sup>3</sup>,  
Alberto Saiani<sup>4</sup>, and Tom Shearer<sup>1</sup>

<sup>1</sup>*Department of Mathematics, School of Natural Sciences, Faculty of Science and Engineering, The University of Manchester, Oxford Road, M13 9PL, UK*

<sup>2</sup>*Department of Materials and Manchester Institute of Biotechnology, School of Natural Sciences, Faculty of Science and Engineering, The University of Manchester, Oxford Road, M13 9PL, UK*

<sup>3</sup>*Department of Chemical Engineering, School of Engineering, Faculty of Science and Engineering, The University of Manchester, Oxford Road, M13 9PL, UK*

<sup>4</sup>*Division of Pharmacy and Optometry and Manchester Institute of Biotechnology, School of Health Sciences, Faculty of Biology, Medicine and Health, The University of Manchester, Oxford Road, M13 9PL, UK*

## Abstract

The structures of fibre networks can vary greatly due to fibre interactions during formation. We have modified the steps of generating Mikado networks to create two new model classes by altering the spatial distribution and relative orientation of their fibres to mimic the structures of self-assembling peptide hydrogels (SAPHs), whose physical properties depend strongly on their fibres' interactions. The results of our models and experiments on a set of beta-sheet forming SAPHs show that modifying a network's structure affects the percolation threshold and the mechanical behaviour of the material, both near percolation and at higher densities.

Many materials are constructed from fibre networks, from biological materials, such as collagen-based tissues and the cytoskeleton, to synthetic materials, such as gels and paper [1]. These materials are often modelled as stochastic networks [2–5] to study their physical properties, such as percolation [6] and elastic modulus [2, 7]. It has been shown that, at densities near percolation, the network’s elastic moduli vary proportionally to  $(\rho - \rho_c)^f$ , where  $\rho$ ,  $\rho_c$ , and  $f$  are the density ( $\rho = N/L^2$ , the number of fibres per unit square area of side length  $L$ ), percolation threshold density, and elastic exponent of the network, respectively [8]. At higher densities ( $\rho \gg \rho_c$ ), they vary proportionally to  $\rho^{f_h}$ , where  $f_h$  is the high density elastic exponent [9, 10].

Researchers have modified various aspects of fibre networks to investigate their material properties. Parvez and Picu [11] investigated network connectivity – the mean number of fibre segments emerging from each node in the network (a segment is the portion of a fibre between two connected nodes). They showed that the elastic modulus in the non-affine regime increases, but the exponent  $f_h$  decreases, with increasing connectivity. The global orientation preference of fibres has also attracted attention [12, 13]. Tarasevich and Eserkepov [12] modified fibre orientation with respect to a global coordinate system to create anisotropic networks and showed that they percolate at higher densities.

Network-based materials form in a wide variety of ways [14], which gives them dissimilar structures. For example, open cell foams differ from collagen gels. Foams are formed by introducing gas bubbles into monomer solution before solidification [15], while collagen gels are formed by cells laying down fibrils which self-assemble [16]. To model the former, it is more suitable to use Voronoi networks, and for the latter, Mikado networks [17].

In this paper, we model self-assembling peptide hydrogels (SAPHs), a family of peptides extensively studied by our group for their self-assembly, gelation, and potential biomedical uses like tissue engineering and drug delivery [18–20]. In SAPHs, fibres formed of short peptide sequences create a network through self-association [21]. The fibres are sufficiently thick and rigid enough to ignore thermal fluctuations. Variations in amino acid sequences or environmental conditions can significantly alter fibre interactions, affecting the network’s structure and mechanical properties, with elastic exponents ranging from 2 to 4.6 [10, 22]. Despite their importance, however, the effects of local fibre interactions on the structure and mechanical behaviour of the network are not fully understood. To understand how the structural changes caused by fibre interactions lead to mechanical changes, we modi-

fied the Mikado network generation process (we did not *directly* model fibre formation, branching and interaction). Our results apply equally to any materials that have similar structures.

Two dimensional Mikado networks are created by randomly and independently placing a given number of fibres of length  $l$  (we used  $l = 1$ ) with random orientation within a square domain of side length  $L$ . We modified this process by changing two fibre features, their distribution in space and their relative orientation, as follows:

- To modify spatial distribution, after randomly determining a position for a fibre's centre, a probability,  $P_e$ , was assigned based on the number of existing fibre centres within a radius,  $r_e$ . A random number between 0 and 1 was then generated, and if it exceeded  $P_e$ , the fibre was deleted.
- To modify orientation, the orientations of fibres within a radius,  $r_\theta$ , were used to define the distribution from which the candidate fibre's orientation was drawn, increasing the likelihood of a specified alignment relative to existing fibres.

The defined probabilities and the critical radii can be specified in various forms. The forms we chose are given below. For the existence probability, we specified

$$P_e = (1 - P_r)^{n_e}, \quad (1)$$

$$r_e = \alpha \sqrt{\frac{1}{\rho}}, \quad (2)$$

where  $P_r$ ,  $n_e$ , and  $\alpha$  are, respectively: the reduction in the probability of the new fibre existing due to the presence of a single fibre centre previously placed within the circle, the number of fibre centres that already exist within that circle, and a constant which scales  $r_e$  relative to  $\sqrt{1/\rho}$ , the distance between nodes in perfect square lattice. In our simulations we chose  $\alpha = 3/4$ . The orientation is chosen, based on the orientations of the existing fibres within a circle of radius  $r_\theta$  (we chose  $r_\theta = l/2$ ), from a Gaussian mixture distribution [23]:

$$g(\theta) = \sum_{i=1}^{n_\theta} \frac{1}{n_\theta} \frac{1}{\sigma \sqrt{2\pi}} \exp\left(-\frac{(\theta - (\theta_{fi} + \Theta))^2}{2\sigma^2}\right), \quad (3)$$

where  $\Theta$ ,  $n_\theta$ ,  $\sigma$ , and  $\theta_{fi}$ , are the preferred orientation relative to the existing fibres, the number of fibres within the circle, the standard deviation of the

Table 1: Parameters used to generate the networks, the critical percolation threshold density,  $\rho_c$ , elastic exponent (from equation (5)),  $f$ , and exponent at high density,  $f_h$ , for the six network classes considered (mean  $\pm$  standard error).

Network type	$P_r$	$\Theta$	$\rho_c l^2$	$f$	$f_h$
Mikado	N/A	N/A	$5.6373 \pm 0.0001$	$3.77 \pm 0.02$	$7.9 \pm 0.1$
DM	0.8	N/A	$4.9919 \pm 0.0002$	$3.56 \pm 0.01$	$7.7 \pm 0.1$
DOM 1	0	$\frac{\pi}{2}$	$4.954 \pm 0.001$	$3.70 \pm 0.01$	$8.4 \pm 0.1$
DOM 2	0.8	$\frac{\pi}{2}$	$4.1907 \pm 0.0001$	$3.53 \pm 0.01$	$8.0 \pm 0.1$
DOM 3	0	0	$9.43 \pm 0.01$	$3.92 \pm 0.02$	$9.6 \pm 0.1$
DOM 4	0.8	0	$7.690 \pm 0.001$	$3.68 \pm 0.02$	$9.0 \pm 0.1$

distribution (we used  $\sigma = 1/\sqrt{12}$ ), and the angle the  $i^{\text{th}}$  fibre makes with the  $x$ -axis, respectively.

We generated and compared three network classes: the unmodified Mikado network, the *distribution-modified* (DM) network, where only spatial distribution is modified, and the *distribution-orientation-modified* (DOM) network, where both spatial distribution and orientation are modified. For the DOM networks, we considered two orientations:  $\Theta = 0$  (which encourages fibres to co-align) and  $\Theta = \pi/2$  (which encourages the fibres to be perpendicular). Networks with the parameters given in Table 1 were studied, and examples of each type are shown in Figure 1.

We first studied percolation. All the subsequent analysis was carried out on percolated systems. Network percolation was investigated based on the finding that  $\rho_{0.5}(L)$  (the density at which the percolation probability is 0.5 for finite  $L$ ) converges to  $\rho_c$  as  $L \rightarrow \infty$  [6, 24, 25], since

$$\rho_{0.5}(L) - \rho_c = -\frac{b_0}{a_1} L^{-1-1/\nu_c} + \dots, \quad (4)$$

where  $\rho_c$ ,  $\nu_c$ ,  $b_0$ , and  $a_1$  are the critical percolation density, the correlation-length exponent (a universal constant that is only affected by dimensionality, which equals 4/3 for 2D systems [6, 8]), and some fitting constants, respectively. We used a method similar to that developed by Pike and Seager [26] to find  $\rho_{0.5}(L)$  (see Supplemental Material for further details).

The percolation thresholds are presented in Table 1. Our results for Mikado networks are consistent with the literature [6, 27]; however, as we modify the spatial dispersion, or make the fibres more likely to be perpendicular,  $\rho_c$  decreases, and if we make the fibres more likely to be parallel,  $\rho_c$

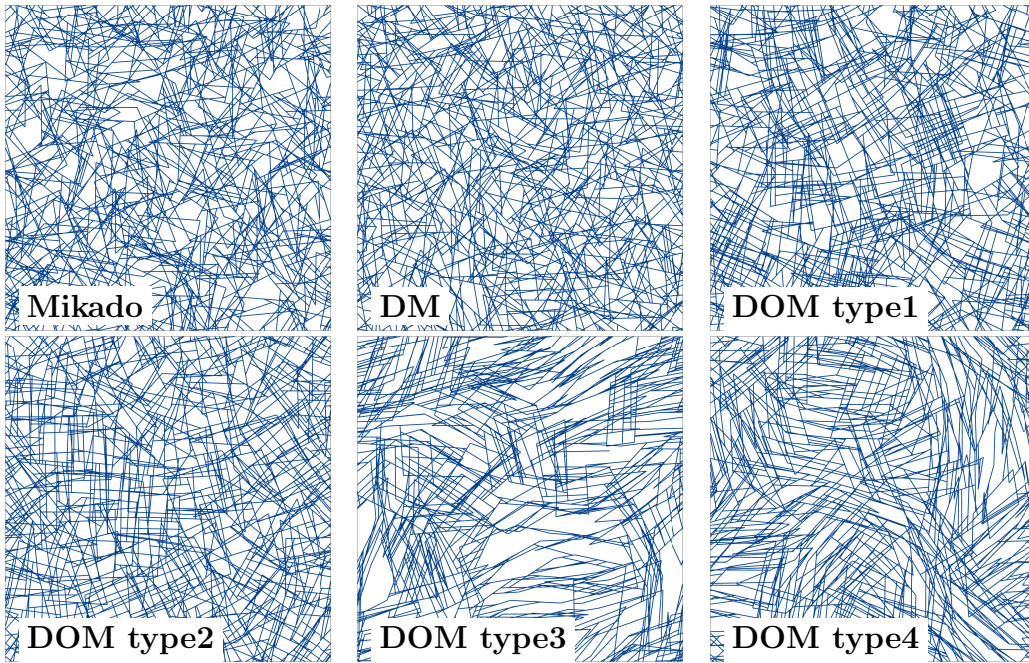


Figure 1: Samples of the studied networks with  $\rho = 30$ ,  $l = 1$ , and  $L = 5$ .

increases.

The second aspect that we investigated was how fibres are dispersed within the domain of study. To do so, we created networks of various densities with  $L = 10$ , divided them into 400 smaller boxes, counted the number of fibre centres in each box, then calculated the mean and variance of this quantity. It is well known that, in Mikado networks, the number of fibre centres in each box follows a Poisson distribution [28] (Figure 2a). An increase in the value of  $P_r$  results in a more homogeneous (lower variance) network.

The connectivity of a network,  $Z$ , plays an important role in the network's behaviour [11]. As depicted in Figure 2b, for more homogeneous networks, the connectivity is slightly lower. The reason for this is fibre clumping (see Figure 1) [28]. As a result, fibres in the vicinity of these clumps have a relatively high chance of forming connections, and thus will have a higher connectivity. Moreover, for the networks whose fibres have a preference for being parallel ( $\Theta = 0$ ), the connectivity is considerably smaller. However, the difference between all network classes vanishes as the density increases.

Two other important geometrical factors are the mean length and density of fibre segments, as plotted in Figures 2c and 2d. Networks with  $\Theta = 0$  have

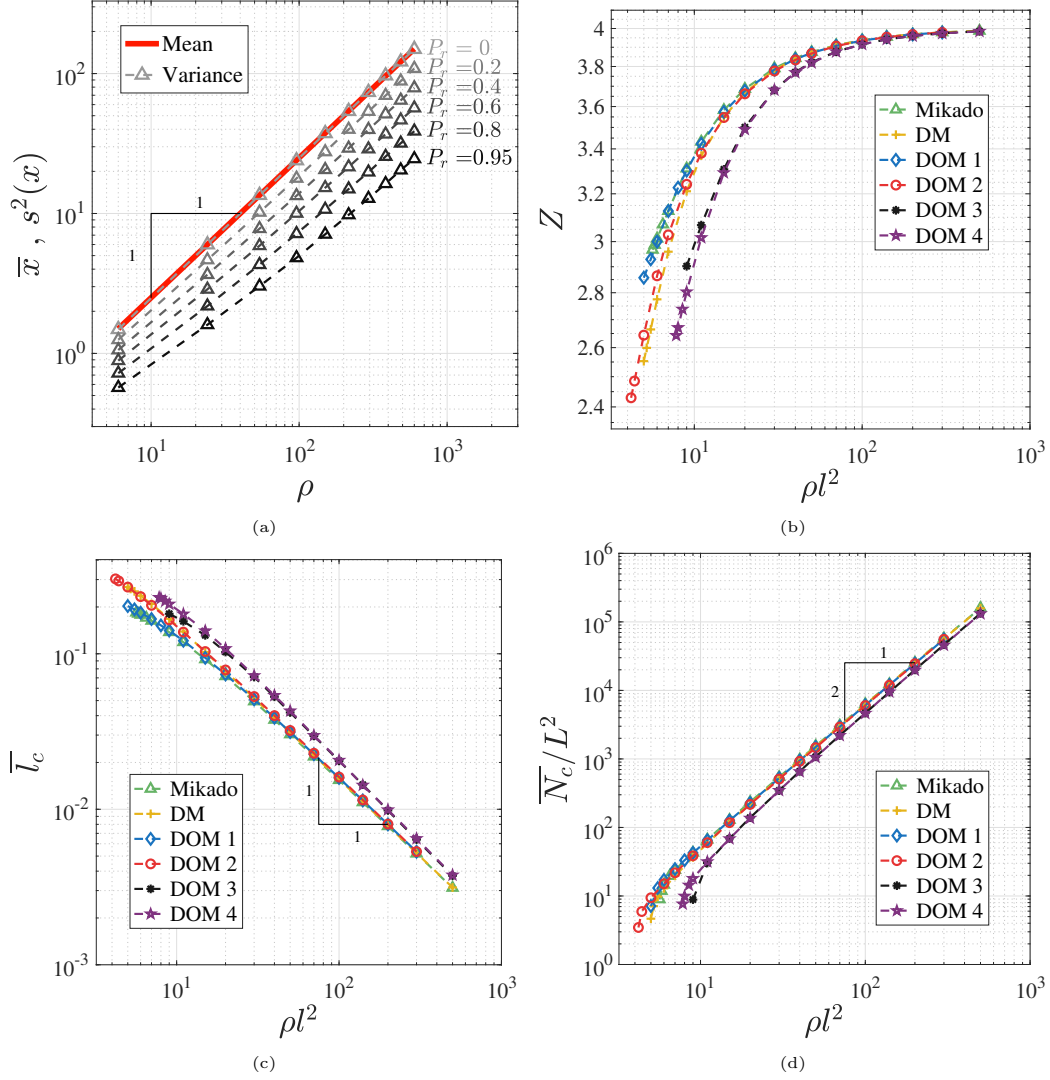


Figure 2: Geometric features of the networks. (a) The mean,  $\bar{x}$ , and variance,  $s^2$ , of the number of fibres in 400 sub-boxes, as described in the text, for Mikado Networks and DM networks with various values of  $P_r$ . (b) The connectivity,  $Z$ , as a function of the dimensionless density,  $\rho l^2$ . (c) The mean segment length,  $\bar{l}_c$ . (d) The mean number of segments per unit area,  $\bar{N}_c/L^2$ . The standard errors for this data are smaller than the size of the markers in all plots.

longer fibre segments and lower segment density but gradually converge with the other networks as  $\rho l^2 \rightarrow \infty$ . It will be shown that this affects the modulus of the networks substantially. In contrast, other network classes converge at lower densities, suggesting relatively similar mechanical responses.

Our investigation into the networks' mechanical properties is divided into the two cases of near percolation and high density [2, 7]. For low densities, the finite size scaling method [7, 8] is used, and at high densities, a representative volume element (RVE) is considered [9]. In this study, the segments of the network are considered to be beams with second moment of area,  $I$  [29], with square cross-sections. The nodes are considered to be stiff cross-links (relative rotation is prohibited between beams connected at a node). The Timoshenko beam model [29] is used to model the beams and the direct stiffness method [29] is used to model infinitesimal deformation of the network.

It has been shown that the following scaling law can be used to describe the relationship between the mean Young's modulus,  $\bar{E}$ , and the size of the network at  $\rho = \rho_c$ , [30]

$$\bar{E} = c_1 L^{-f/\nu_c}, \quad (5)$$

where  $c_1$  is a fitting constant. This is equivalent to  $-\frac{\ln \bar{E}}{\ln L} = \frac{f}{\nu_c} - \frac{\ln c_1}{\ln L}$ . By calculating  $\bar{E}$  for various system sizes, and using a plot with  $-\frac{\ln \bar{E}}{\ln L}$  and  $\frac{1}{\ln L}$  as the axes, the intersection of the fitted curve with the  $-\frac{\ln \bar{E}}{\ln L}$  axis is  $\frac{f}{\nu_c}$ .

To calculate the elastic modulus, a displacement in the  $y$ -direction was applied to each node on the top boundary, while the displacement in the  $x$ -direction and rotation were fixed. On the bottom boundary, zero displacement and rotation was imposed, and on the lateral boundaries, zero force was imposed. The number of realisations varied with system size from 1,600 for the largest to 102,600 for the smallest.

The results are presented in Table 1. For the Mikado networks, the value of the elastic exponent was calculated as  $f = 3.73 \pm 0.02$ . This is different from a previously reported value,  $f = 3.2 \pm 0.3$  [2, 7], due to our use of a more accurate value for the percolation threshold. Our results show that the various network types considered here have different elastic exponents. This suggests that materials whose fibres interact during formation, thus modifying the structure of the network, belong to different universality classes.

It has been shown that, at high density, the behaviour of fibre networks can be divided into two regimes: affine and non-affine [2, 7, 9]. In the non-affine regime, the bending stiffness of the fibre segments is much smaller than their stretching stiffness. In the affine regime, the network elastic moduli vary

linearly with density and in the non-affine regime, they vary proportionally to  $(\rho l)^{f_h} (l_b/l)^2$ , where  $l_b = \sqrt{I/A}$ , and  $A$  is the fibre cross-sectional area [9].

To determine the shear modulus,  $G$ , of the simulated networks, a periodic boundary condition with a far-field simple shear deformation was applied in a manner that is explained in depth by Nguyen et al. [31]. In order to find  $f_h$  for different network types, we simulated networks with a fibre thickness of 0.0001 and densities ranging from 25 to 500; the results are presented in Figure 3a. For the Mikado network,  $f_h$  was found to be 7.9, as reported in the literature [9, 32]. The other values are presented in Table 1. Increasing the spatial dispersion of fibres slightly decreases the value of  $f_h$ . Furthermore, noticeable changes can be observed for networks with preferred parallel orientations. It is likely that all of the geometrical features discussed in Figure 2 impact the network mechanical moduli, but disentangling every specific relationship between structure and mechanics is not straightforward. However, as can be seen from Figures 2b-d, for DOM type 3 and 4 networks, the connectivity is lower, and the gradients of the mean segment length and the mean segment density are steeper; which, in the bending-dominated regime, causes the value of  $f_h$  to be higher.

The value of  $G$  varies significantly between the six network types. It can vary up to 50 times in the bending-dominated regime. For DOM type 3 and 4 networks,  $G$  is smaller by at least one order of magnitude in the non-affine regime. This is due to their lower connectivity and segment density, and higher segment length. This clearly shows how influential network structure is on the mechanical behaviour of fibrous materials.

We also investigated the Poisson's ratio,  $\nu$ , of our six network types. To do so, we applied boundary conditions that impose a pure longitudinal deformation, and calculated the total forces in the directions parallel and perpendicular to the direction of stretch; Poisson's ratio is then calculated using  $\nu = F_{\perp}/F_{\parallel}$ , where  $F_{\perp}$  and  $F_{\parallel}$  are the total perpendicular and parallel forces at the boundary interfaces (see Supplemental Material for a derivation). We display the effects of changing the density,  $\rho$ , and  $l_b$ , in Figure 3b. There is a noticeable difference in the value of  $\nu$  between the different networks, which is more pronounced when the relative orientations of the fibres change.

The Poisson's ratio in the non-affine regime is not constant and changes with increasing density. This is contrary to previous papers that reported  $\nu$  to be constant [2, 32]. The effect on  $\nu$  of increasing density diminishes into the affine regime (as far as we have made observations). The effect of  $l_b$ ,



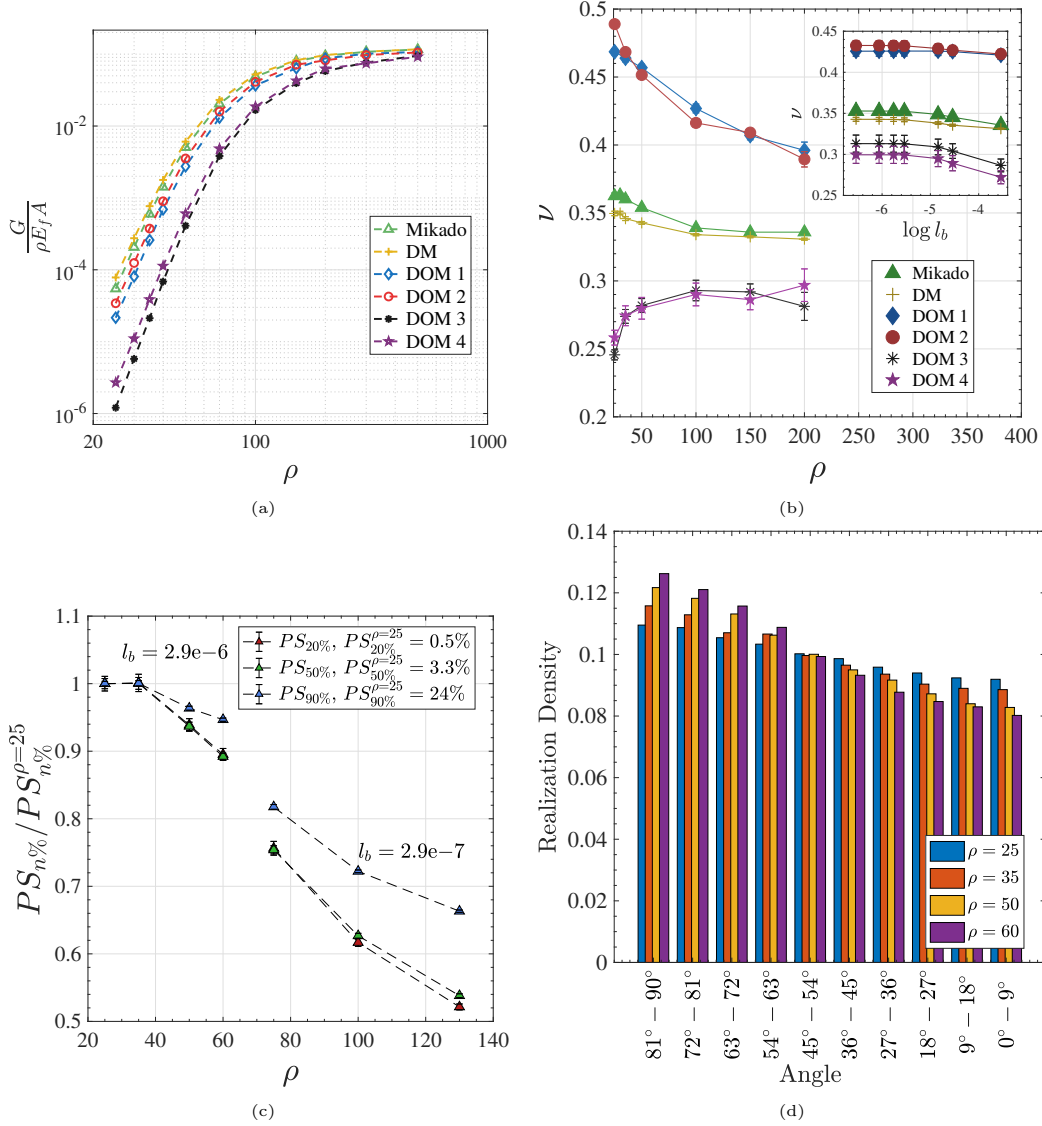


Figure 3: (a) Shear modulus as a function of density for high density networks ( $E_f$  is the fibre Young's modulus). (b) The dependence of Poisson's ratio on density and  $l_b$ . For the main figure  $l_b = 2.9e-5$ . In the inset panel,  $\rho = 75$ . (c)  $PS_{n\%}$  represents the smallest possible proportion of a network's segments that together store  $n\%$  of the total energy in the network.  $PS_{n\%}^{\rho=25}$  represents  $PS_{n\%}$  with  $\rho = 25$ . All the data in this figure is for Mikado networks in the non-affine regime. (d) Histogram of the orientations of fibres relative to the horizontal axis (which is perpendicular to the stretch direction) that carry 50% of the energy in each Mikado network. The absolute value of each angle has been taken. This data is for  $l_b = 2.9e-6$ .

however, is different; in the non-affine regime, increasing it has no effect, but as we transition into the affine regime, increasing it reduces the value of  $\nu$  as far as we have made observations.

The reason for the effect of density on  $\nu$ , even when the network remains in the non-affine regime, lies in how the network absorbs energy at different densities. We have demonstrated this for Mikado networks by looking at two parameters: the percentage of segments that carry a given percentage of the total energy absorbed by the network, and the orientations of these fibres. The results are presented in Figures 3c and 3d. The percentage of segments involved in absorbing a given portion of the total energy decreases with increasing density. The orientation distribution of these fibres also noticeably changes. In Figure 3d, we can see that, at higher densities, the segments have a greater preference to be parallel to the stretch direction (in all cases the energy absorbed through stretching is negligible). The reason for the change in the energy distribution is unclear, but it can be inferred that this change is rooted in how the microstructure deforms and this, in turn, affects the Poisson's ratio.

To compare the results of the model networks qualitatively with real SAPHs, we carried out shear rheometry tests on three  $\beta$ -sheet forming peptides: KFEFEFKFK**F** (F), KFEFEFKFK**K** (K), and KFEFEFKFK**FK** (FK) (K: lysine; F: phenylalanine; E: glutamic acid). These peptides are based on a design first developed by Zhang et al. [33], Zhang and Altman [34] (see the Supplemental Material for details). Figure 4a-c shows transmission electron microscopy (TEM) images obtained for 10 $\times$  diluted hydrogels alongside the chemical structure of the SAPHs. These images confirm the formation in all three systems of semi-rigid peptide fibre networks with the thinnest fibre diameter ranging from 3 to 4 nm. Wychowanec et al. [22] have shown that peptides with hydrophobic end-groups (F) have more hydrophobic edge interactions and are thought, therefore, to form more crosslinks. These networks are thus more similar to the perpendicular network model described above. On the other hand, peptides with hydrophilic (K) end-groups were shown to make fewer crosslinks due to edge electrostatic repulsion and, therefore, will be more similar to the parallel network model. In Figure 4d, the storage moduli,  $G'$ , obtained for these three hydrogels are presented. For FK and K hydrogels, similar exponents ( $2.4 \pm 0.2$ ) were obtained. Both these systems have fibres with hydrophilic edges due to the presence of the terminal K. FK was found to have a higher  $G'$  compared to K which can be attributed to the presence of the additional phenylalanine group before

the terminal K. This additional F increases the overall hydrophobicity of the peptides and the intermolecular forces (H-bond number) between peptides, resulting in more rigid fibres with higher moduli, without affecting the exponent. For the F hydrogels, significantly higher values of  $G'$  were observed (due to higher crosslinking levels) with a smaller exponent, as predicted by the models.

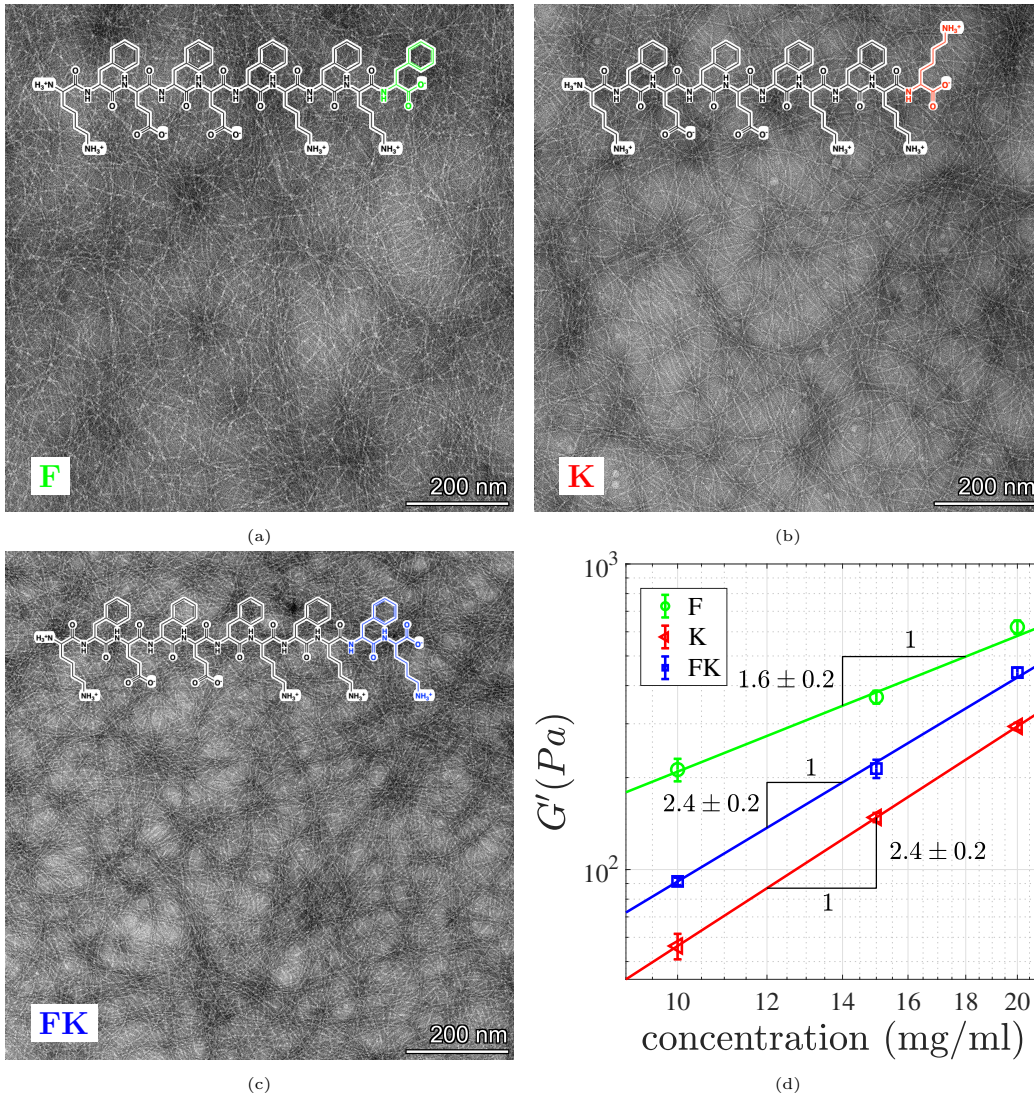


Figure 4: (a)-(c) TEM images of three SAPHs with  $10\times$  dilution in  $57000\times$  magnification, and their chemical structure (inset). (d) Rheology test results for the SAPHs;  $G'$ , the storage modulus, versus peptide concentration (which is a proxy for  $\rho l$  in the models due to the one-to-one relationship between the mass and length of a peptide fibre).

In conclusion, to investigate the effects of network structure on material properties, new networks based on Mikado networks were created and studied at low (near percolation) and high densities. Their behaviours were shown to be affected by localised modifications, which represent the existence of local interactions between the fibres when the network is forming. We found

that increasing spatial dispersion, and modifying orientation such that fibres have a greater tendency to intersect, decreases the percolation threshold and elastic exponent near the percolation threshold. At high densities, in the non-affine regime, the trends in the model networks' shear moduli agreed with experiments we conducted on real SAPHs. Finally, we showed that the Poisson's ratio depends on both the deformation regime and the density. The reason for this lies in how the networks absorb energy at different densities.

## References

- [1] Catalin R. Picu. *Introduction: Definitions and Classification*, page 1–12. Cambridge University Press, 2022.
- [2] David A. Head, Alex J. Levine, and F. C. MacKintosh. Deformation of cross-linked semiflexible polymer networks. *Physical Review Letters*, 91(10), 2003. doi: 10.1103/PhysRevLett.91.108102.
- [3] Stefan B. Lindström. Biopolymer network geometries: Characterization, regeneration, and elastic properties. *Physical Review E*, 82(5), 2010. doi: 10.1103/PhysRevE.82.051905.
- [4] Anne S. G. van Oosten, Mahsa Vahabi, Albert J. Licup, Abhinav Sharma, Peter A. Galie, Fred C. MacKintosh, and Paul A. Janmey. Uncoupling shear and uniaxial elastic moduli of semiflexible biopolymer networks: compression-softening and stretch-stiffening. *Scientific Reports*, 6(1), jan 2016. doi: 10.1038/srep19270. URL <https://doi.org/10.1038/srep19270>.
- [5] Dylan T. Casey, Samer Bou Jawde, Jacob Herrmann, Vitor Mori, J. Matthew Mahoney, Béla Suki, and Jason H. T. Bates. Percolation of collagen stress in a random network model of the alveolar wall. *Scientific Reports*, 11(1), aug 2021. doi: 10.1038/s41598-021-95911-w. URL <https://doi.org/10.1038/s41598-021-95911-w>.
- [6] Jiantong Li and Shi Li Zhang. Finite-size scaling in stick percolation. *Physical Review E - Statistical, Nonlinear, and Soft Matter Physics*, 80, 2009. ISSN 15393755. doi: 10.1103/PhysRevE.80.040104.

- [7] Jan Wilhelm and Erwin Frey. Elasticity of stiff polymer networks. *Physical Review Letters*, 91(10), 2003. doi: 10.1103/PhysRevLett.91.108103.
- [8] Dietrich Stauffer and Ammon Aharony. *Introduction To Percolation Theory*. Taylor & Francis, dec 2018. doi: 10.1201/9781315274386. URL <https://doi.org/10.1201/9781315274386>.
- [9] A.S. Shahsavari and R.C. Picu. Size effect on mechanical behavior of random fiber networks. *International Journal of Solids and Structures*, 50(20):3332–3338, 2013. ISSN 0020-7683. doi: <https://doi.org/10.1016/j.ijsolstr.2013.06.004>. URL <https://www.sciencedirect.com/science/article/pii/S0020768313002382>.
- [10] Jie Gao, Claire Tang, Mohamed A. Elsayy, Andrew M. Smith, Aline F. Miller, and Alberto Saiani. Controlling self-assembling peptide hydrogel properties through network topology. *Biomacromolecules*, 18, 2017. ISSN 15264602. doi: 10.1021/acs.biomac.6b01693.
- [11] Nishan Parvez and Catalin R. Picu. Effect of connectivity on the elasticity of athermal network materials. *Soft Matter*, 19:106–114, 2023. doi: 10.1039/D2SM01303G. URL <http://dx.doi.org/10.1039/D2SM01303G>.
- [12] Yuri Yu. Tarasevich and Andrei V. Eserkepov. Percolation of sticks: Effect of stick alignment and length dispersity. *Phys. Rev. E*, 98:062142, Dec 2018. doi: 10.1103/PhysRevE.98.062142. URL <https://link.aps.org/doi/10.1103/PhysRevE.98.062142>.
- [13] Thomas Ackermann, Raphael Neuhaus, and Siegmund Roth. The effect of rod orientation on electrical anisotropy in silver nanowire networks for ultra-transparent electrodes. *Scientific Reports*, 6(1):34289, 2016. doi: 10.1038/srep34289. URL <https://doi.org/10.1038/srep34289>.
- [14] Catalin R. Picu. *Introduction: Definitions and Classification*, pages 1–12. Cambridge University Press, 2022. doi: 10.1017/9781108779920.002.
- [15] Lorna J. Gibson and Michael F. Ashby. *The structure of cellular solids*, pages 15–51. Cambridge Solid State Science Series. Cambridge University Press, 2 edition, 1997. doi: 10.1017/CBO9781139878326.004.

- [16] Shichen Zhu, Qijuan Yuan, Tao Yin, Juan You, Zhipeng Gu, Shanbai Xiong, and Yang Hu. Self-assembly of collagen-based biomaterials: preparation, characterizations and biomedical applications. *J. Mater. Chem. B*, 6:2650–2676, 2018. doi: 10.1039/C7TB02999C. URL <http://dx.doi.org/10.1039/C7TB02999C>.
- [17] M. R. Islam and R. C. Picu. Effect of network architecture on the mechanical behavior of random fiber networks. *Journal of Applied Mechanics*, 85(8), jun 2018. doi: 10.1115/1.4040245. URL <https://doi.org/10.1115%2F1.4040245>.
- [18] Faye Bolan, Ben R Dickie, James R Cook, Josephine M Thomas, Emmanuel Pinteaux, Stuart M Allan, Alberto Saiani, and Catherine B Lawrence. Intracerebral administration of a novel self-assembling peptide hydrogel is safe and supports cell proliferation in experimental intracerebral haemorrhage. *Translational stroke research*, 15(5):986–1004, 2024.
- [19] Mohamed A Elsayy, Jacek K Wychowaniec, Luis A Castillo Díaz, Andrew M Smith, Aline F Miller, and Alberto Saiani. Controlling doxorubicin release from a peptide hydrogel through fine-tuning of drug-peptide fiber interactions. *Biomacromolecules*, 23(6):2624–2634, 2022.
- [20] Eliana Lingard, Siyuan Dong, Anna Hoyle, Ellen Appleton, Alis Hales, Eldhose Skaria, Craig Lawless, Isobel Taylor-Hearn, Simon Saadati, Qixun Chu, et al. Optimising a self-assembling peptide hydrogel as a matrigel alternative for 3-dimensional mammary epithelial cell culture. *Biomaterials Advances*, 160:213847, 2024.
- [21] Mohamed A. Elsayy, Andrew M. Smith, Nigel Hodson, Adam Squires, Aline F. Miller, and Alberto Saiani. Modification of  $\beta$ -sheet forming peptide hydrophobic face: Effect on self-assembly and gelation. *Langmuir*, 32, 2016. ISSN 15205827. doi: 10.1021/acs.langmuir.5b03841.
- [22] Jacek K. Wychowaniec, Andrew M. Smith, Cosimo Ligorio, Oleksandr O. Mykhaylyk, Aline F. Miller, and Alberto Saiani. Role of sheet-edge interactions in  $\beta$ -sheet self-assembling peptide hydrogels. *Biomacromolecules*, 21(6):2285–2297, 06 2020. doi: 10.1021/acs.biomac.0c00229. URL <https://doi.org/10.1021/acs.biomac.0c00229>.

- [23] Marc Peter Deisenroth, A. Aldo Faisal, and Cheng Soon Ong. *Mathematics for Machine Learning*. Cambridge University Press, 2020.
- [24] Robert M. Ziff. Spanning probability in 2d percolation. *Phys. Rev. Lett.*, 69:2670–2673, Nov 1992. doi: 10.1103/PhysRevLett.69.2670. URL <https://link.aps.org/doi/10.1103/PhysRevLett.69.2670>.
- [25] R. M. Ziff and M. E. J. Newman. Convergence of threshold estimates for two-dimensional percolation. *Phys. Rev. E*, 66:016129, Jul 2002. doi: 10.1103/PhysRevE.66.016129. URL <https://link.aps.org/doi/10.1103/PhysRevE.66.016129>.
- [26] G. E. Pike and C. H. Seager. Percolation and conductivity: A computer study. i. *Physical Review B*, 10, 1974. ISSN 01631829. doi: 10.1103/PhysRevB.10.1421.
- [27] Stephan Mertens and Cristopher Moore. Continuum percolation thresholds in two dimensions. *Physical Review E—Statistical, Nonlinear, and Soft Matter Physics*, 86(6):061109, 2012.
- [28] William Wyatt Sampson. *Modelling Stochastic Fibrous Materials with Mathematica®*, volume 53. Springer, 2009.
- [29] Daryl L Logan. *A First Course in the Finite Element Method Sixth Edition*. Thomson, 2016.
- [30] JG Zabolitzky, DJ Bergman, and D Stauffer. Precision calculation of elasticity for percolation. *Journal of statistical physics*, 44:211–223, 1986.
- [31] V.-D. Nguyen, E. Béchet, C. Geuzaine, and L. Noels. Imposing periodic boundary condition on arbitrary meshes by polynomial interpolation. *Computational Materials Science*, 55:390–406, 2012. ISSN 0927-0256. doi: <https://doi.org/10.1016/j.commatsci.2011.10.017>. URL <https://www.sciencedirect.com/science/article/pii/S0927025611005866>.
- [32] A. Shahsavari and R. C. Picu. Model selection for athermal cross-linked fiber networks. *Phys. Rev. E*, 86:011923, Jul 2012. doi: 10.1103/PhysRevE.86.011923. URL <https://link.aps.org/doi/10.1103/PhysRevE.86.011923>.



- [33] Shuguang Zhang, Todd Holmes, Curtis Lockshin, and Alexander Rich. Spontaneous assembly of a self-complementary oligopeptide to form a stable macroscopic membrane. *Proceedings of the National Academy of Sciences*, 90(8):3334–3338, 1993.
- [34] Shuguang Zhang and Michael Altman. Peptide self-assembly in functional polymer science and engineering. *Reactive and Functional Polymers*, 41(1-3):91–102, 1999.

Supplemental material for  
 “The effects of fibre spatial distribution and  
 relative orientation on the percolation and  
 mechanics of stochastic fibre networks: A  
 model of peptide hydrogels”

Amir Hossein Namdar<sup>1</sup>, Nastaran Zoghi<sup>2</sup>, Aline Miller<sup>3</sup>,  
 Alberto Saiani<sup>4</sup>, and Tom Shearer<sup>1</sup>

<sup>1</sup>*Department of Mathematics, School of Natural Sciences, Faculty of Science and Engineering, The University of Manchester, Oxford Road, M13 9PL, UK*

<sup>2</sup>*Department of Materials and Manchester Institute of Biotechnology, School of Natural Sciences, Faculty of Science and Engineering, The University of Manchester, Oxford Road, M13 9PL, UK*

<sup>3</sup>*Department of Chemical Engineering, School of Engineering, Faculty of Science and Engineering, The University of Manchester, Oxford Road, M13 9PL, UK*

<sup>4</sup>*Division of Pharmacy and Optometry and Manchester Institute of Biotechnology, School of Health Sciences, Faculty of Biology, Medicine and Health, The University of Manchester, Oxford Road, M13 9PL, UK*

## 1 Percolation and elastic moduli exponent calculations

The percolation probability, for a system with given side length,  $L$ , with density,  $\rho$ , near the percolation threshold, is [6,24,25]

$$R(\rho, L) = \frac{b_0}{L} + 0.5 + a_1 y + a_2 y^3 + \dots, \quad (1)$$

where  $y = (\rho - \rho_c)L^{1/\nu_c} \ll 1$ , and  $\rho_c$ ,  $\nu_c$ ,  $b_0$ ,  $a_1$ , and  $a_2$  are the critical percolation density, the correlation-length exponent, and some fitting constants, respectively. From this equation, we deduce that [6,24,25]

$$\rho_{0.5}(L) - \rho_c = -\frac{b_0}{a_1}L^{-1-1/\nu_c} + \dots, \quad (2)$$

where  $\rho_{0.5}(L)$  is the density at which the probability of percolation is 0.5 for a system of size  $L$ . We have neglected higher order terms (which is reasonable when  $\rho$  is close enough to  $\rho_c$  that  $(\rho - \rho_c)^{2n+1}L^{2n/\nu_c}$  is negligible  $\forall n \in \mathbb{N}$ ). Once  $\rho_{0.5}(L)$  is known for several system sizes, it is possible to calculate the percolation density to a desired accuracy using this equation. To calculate  $\rho_{0.5}(L)$ , we started with a system with  $L = 1$  and added a number of fibres (we chose to use 500, 1000 and 5000 fibres to give three data points for each network type). We adjusted the length of the fibres,  $l$ , until the probability of percolation equaled 0.5. To do this, we first roughly estimated the value of  $l$  (by doing a small number of simulations using trial and error to find a value of  $l$  that gave a percolation probability close to 0.5 with a relatively high margin of error), we then considered six values of  $l$  around the roughly estimated value, making  $10^5$  (when there were 5000 fibres) or  $10^6$  (when there were 500 or 1000 fibres) system observations for each value of  $l$ , and then calculated the value of  $l$  that corresponded to a percolation probability of 0.5 by interpolating between these values. Next, we scaled the whole system to make  $l = 1$  and found the corresponding values of  $L$  and  $\rho_{0.5}(L)$  [26]. The values of  $\rho_{0.5}(L)/\rho_c$  for our different network types are plotted in Figure 1.

It is known that the values of the elastic moduli of networks near percolation change exponentially with density; for example, for the Young's modulus,  $E \propto (\rho - \rho_c)^f$ . In order to have a good estimate of  $E$  at each density, the system size must be much larger than the correlation length,  $\xi$ . Precisely at the percolation density,  $\xi = \infty$ , but as the density increases, the correlation length decays as  $\xi \propto (\rho - \rho_c)^{-\nu_c}$  [8]. Therefore, the correlation length is very large near the percolation threshold, so directly investigating the behaviour of such networks is impractical. To overcome this issue, finite size scaling methods have been adopted. It has been shown that the following scaling law can be used to describe the relationship between the elastic moduli and the size of the network at  $\rho = \rho_c$  [30],

$$\overline{E} = c_1 L^{-f/\nu_c}, \quad (3)$$

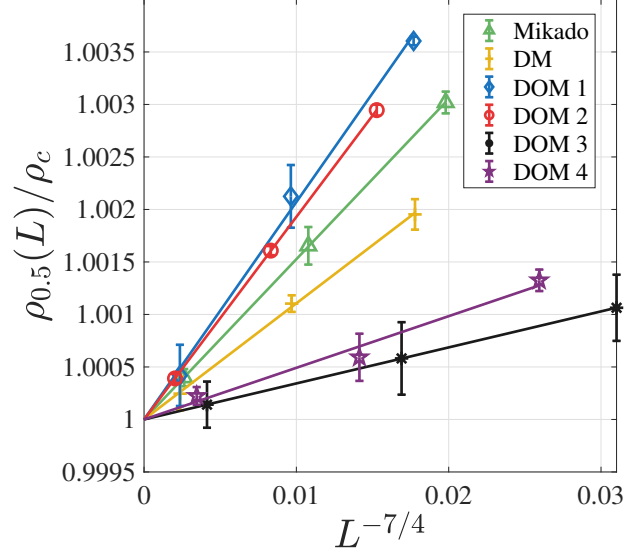


Figure 1: Convergence of  $\rho_{0.5}$  to  $\rho_c$ : as  $L \rightarrow \infty$ ,  $L^{-7/4} \rightarrow 0$  and  $\rho_{0.5}/\rho_c \rightarrow 1$ . The exponent  $-7/4$  comes from equation (2), since  $\nu_c = 4/3$  for two dimensional networks [6, 8].

where  $\bar{E}$  and  $c_1$  are the mean of  $E$  and a constant, respectively. This is equivalent to

$$-\frac{\ln \bar{E}}{\ln L} = \frac{f}{\nu_c} - \frac{\ln c_1}{\ln L}. \quad (4)$$

By calculating  $\bar{E}$  for  $\rho = \rho_c$ , with various system sizes (only considering cases where the system is percolated), and using a plot with  $-\frac{\ln \bar{E}}{\ln L}$  and  $\frac{1}{\ln L}$  as the axes, the intersection of the fitted curve with the  $-\frac{\ln \bar{E}}{\ln L}$  axis will be  $f/\nu_c$ . For the Mikado network class, the fitted line is plotted in Figure 2.

## 2 Poisson's ratio

In order to calculate the value of Poisson's ratio,  $\nu$ , we used Hooke's law in 2D,

$$\begin{aligned} \varepsilon_{11} &= \frac{1}{E}(\sigma_{11} - \nu\sigma_{22}), \\ \varepsilon_{22} &= \frac{1}{E}(\sigma_{22} - \nu\sigma_{11}), \\ \varepsilon_{12} &= \frac{1+\nu}{2E}\sigma_{12}, \end{aligned} \quad (5)$$

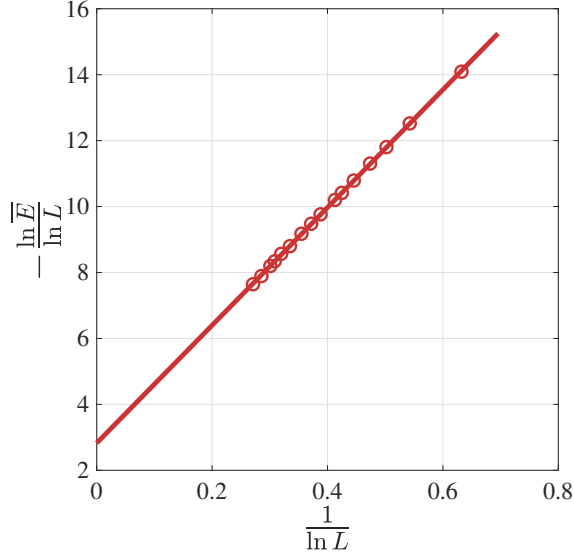


Figure 2: The mean elasticity modulus,  $\bar{E}$ , for Mikado network with  $l = 1$  and *thickness* = 0.001 at various system sizes have been calculated and plotted. As mentioned in the text, they form a straight line in  $-\frac{\ln \bar{E}}{\ln L}$  and  $\frac{1}{\ln L}$  coordinates and the intercept is equal to  $f/\nu_c$ . The standard error for each data point is smaller than the markers.

where  $\varepsilon_{ij}$  and  $\sigma_{ij}$  are the  $ij$ -th components of the strain and stress tensors, respectively, and  $E$  is the material's Young's modulus.

When we apply a purely longitudinal deformation in the  $x_2$  direction,  $\varepsilon_{11}$  and  $\varepsilon_{12}$  will be zero; therefore, we have

$$\nu = \frac{\sigma_{11}}{\sigma_{22}}. \quad (6)$$

Since  $\sigma_{11}$  and  $\sigma_{22}$  are the normal stresses acting on surfaces whose normal vectors are perpendicular and parallel to direction of the uniaxial deformation, respectively, and the fact that we are applying small deformations to a square domain, we can write

$$\nu = \frac{F_{\perp}}{F_{\parallel}}. \quad (7)$$

### 3 Self-assembling peptide hydrogels

The self-assembling peptide hydrogels (SAPHs) we used in our experiments are based on a design first developed by Zhang and coworkers [33-34], with

alternating hydrophilic and hydrophilic residues. The design has been shown to result in peptides that self-assemble into antiparallel  $\beta$ -sheets with all the hydrophobic side groups being located on the same face of the  $\beta$ -sheet, while all the hydrophilic residues are located on the opposite face. It is hypothesised that, in water, two  $\beta$ -sheets come together to bury their hydrophobic faces resulting in the formation of relatively thick and rigid elemental fibres that, under appropriate conditions, associate/interact to form fibrillar networks, i.e. hydrogels. In Figure 3, a schematic representation of the self-assembly and gelation process of these peptides is shown. The peptides form almost perfectly straight fibres. The fibres are sufficiently thick that thermal fluctuations can be neglected in our models.

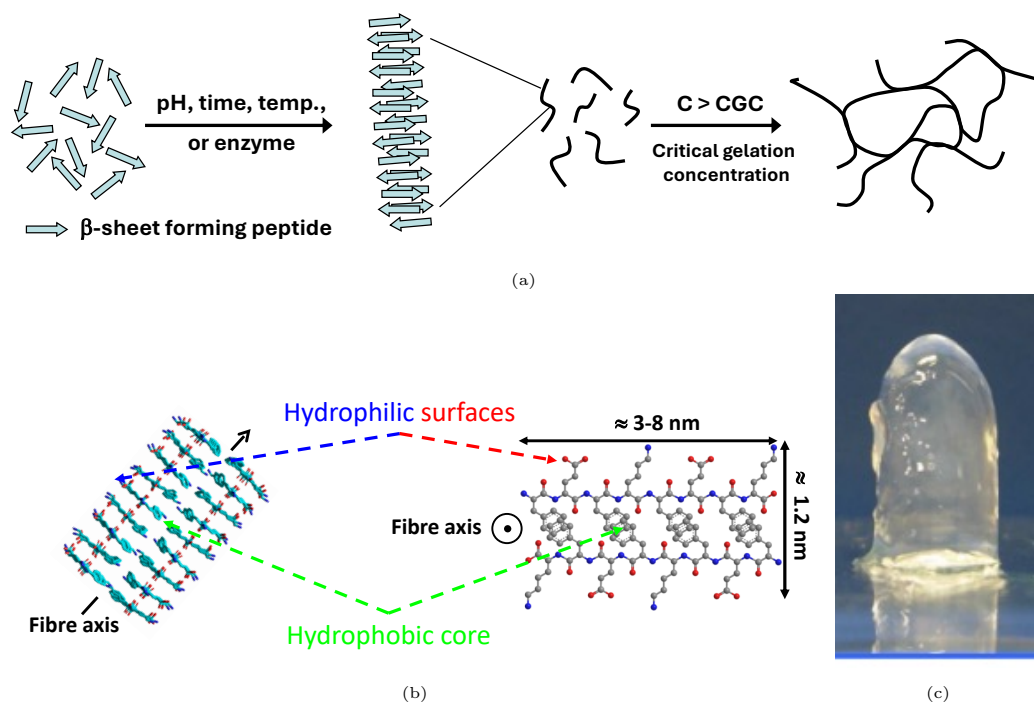


Figure 3: Schematic representation of (a) the self-assembly and gelation pathway of  $\beta$ -sheet forming peptides and (b) the fibres formed (side and top views). (c) Photograph of hydrogel.

## 4 Materials and Methods

### 4.1 Materials:

Peptides (over 95% purity, HCl salts) were obtained from Biomatik LLC (Wilmington, Delaware, USA) and stored at -20°C.

### 4.2 Hydrogel Preparation

Peptides were dissolved in high-performance liquid chromatography-grade water and mixed using a vortexer. The pH was adjusted with NaOH, followed by vortexing and gentle centrifugation to remove bubbles. The overall charge of a peptide can be calculated to be

$$|Z| = \sqrt{\left( \sum_i \frac{N_i \cdot 10^{\text{pK}_{a_i}}}{10^{\text{pH}} + 10^{\text{pK}_{a_i}}} - \sum_j \frac{N_j \cdot 10^{\text{pH}}}{10^{\text{pH}} + 10^{\text{pK}_{a_j}}} \right)^2} \quad (8)$$

where  $N_{i/j}$  represent the numbers and  $\text{pK}_{a_{(i/j)}}$  are the  $\text{pK}_a$  values of the basic (i:  $\text{pK}_a > 7$ ) and acidic (j:  $\text{pK}_a < 7$ ) groups present, respectively [22].

The peptides in this study contain the following ionizable groups:

- carboxylic acid groups ( $\text{COOH}/\text{COO}^-$ ) at the C-terminus ( $\text{pK}_a$  1.83 for F and 2.18 for K) and on glutamic acid side chains ( $\text{pK}_a$  4.25);
- amine groups ( $\text{NH}_3^+/\text{NH}_2$ ) at the N-terminus ( $\text{pK}_a$  8.95) and on lysine side chains ( $\text{pK}_a$  10.53).

Figure 4 shows the theoretical charge of the peptides as a function of pH, with the  $\text{pK}_a$  values of the different ionizable groups indicated. To ensure valid comparisons among the hydrogels, all were prepared to carry a charge of +2. Based on theoretical charge curves, peptides K and FK naturally align at +2 at pH 7, while peptide F, which has a charge of +1 at pH 7, was adjusted to pH 4.25 to achieve the target charge of +2.

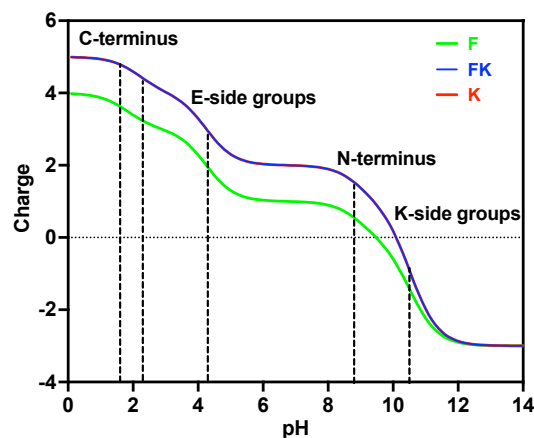


Figure 4: The theoretical charge of the peptides as a function of pH.

### 4.3 Transmission Electron Microscopy (TEM)

TEM images were obtained from 10-fold diluted peptide hydrogels (10 mg/mL, charge +2). A 400-mesh carbon-coated copper grid (EM Resolutions, UK) was floated on a 10  $\mu$ L droplet of the sample for 1 minute, followed by washing with water and staining with 1% uranyl acetate for 30 seconds. After drying, the grid was imaged using a Talos L120C electron microscope.

### 4.4 Oscillatory Rheology

Rheological measurements were performed with a DHR-2 rheometer (20 mm parallel plate, 500  $\mu$ m gap). An amplitude sweep (0.1–100% strain, 1 Hz) determined the linear viscoelastic region (LVR), followed by a frequency sweep (0.2% strain, 0.01–15 Hz) to analyse moduli. The storage modulus at 1 Hz and 0.2% strain (in LVR) was recorded for each sample. Measurements were repeated three times for reproducibility.